

1

Indirect Dark Matter Detection with Cosmic Antimatter

Pierre Salati^a, Fiorenza Donato^b, Nicolao Fornengo^b

^a Laboratoire d'Annecy-le-Vieux de Physique Théorique (LAPTH), CNRS-IN2P3
Université de Savoie, Chemin de Bellevue, 74000 Annecy-le-Vieux Cedex 09, France

^b Dipartimento di Fisica Teorica, Università di Torino
and INFN-Sezione di Torino, Via P. Giuria 1, 10122 Torino, Italy

1.1 Production of antimatter in the galaxy

The indirect detection of particle dark matter (DM) is based on the search for anomalous components in cosmic rays (CRs) due to the annihilation of DM pairs in the galactic halo, on the top of the standard astrophysical production. These additional exotic components are potentially detectable at Earth as spectral distortions for the various cosmic radiations:

$$\chi + \chi \rightarrow q\bar{q}, W^+W^-, \dots \rightarrow \bar{p}, \bar{D}, e^+ \gamma \& \nu' s . \quad (1.1)$$

Detection of the DM annihilation products has motivated the spectacular development of several new experimental techniques. They range from detectors on balloons or in space for the study of antimatter and gamma-rays, to large area cosmic-ray and gamma-ray detectors on the ground to neutrino telescopes underground for the study of the neutrino component. In the following, we will discuss in detail the antimatter component of DM indirect searches, namely antiprotons, antideuterons, and positrons.

1.2 Propagation of antinuclei in the Galaxy

Whatever the mechanism responsible for their production, charged cosmic rays subsequently propagate through the galactic magnetic field and are deflected by its irregularities : the Alfvén waves. In the regime where the magnetic turbulence is strong – which is the case for the Milky Way – Monte Carlo simulations (40) indicate that it is similar to space diffusion with a coefficient:

$$K(E) = K_0 \beta (\mathcal{R}/1 \text{ GV})^\delta , \quad (1.2)$$

which increases as a power law with the rigidity $\mathcal{R} = pc/Ze$ of the particle. In addition, because the scattering-centers drift inside the Milky Way

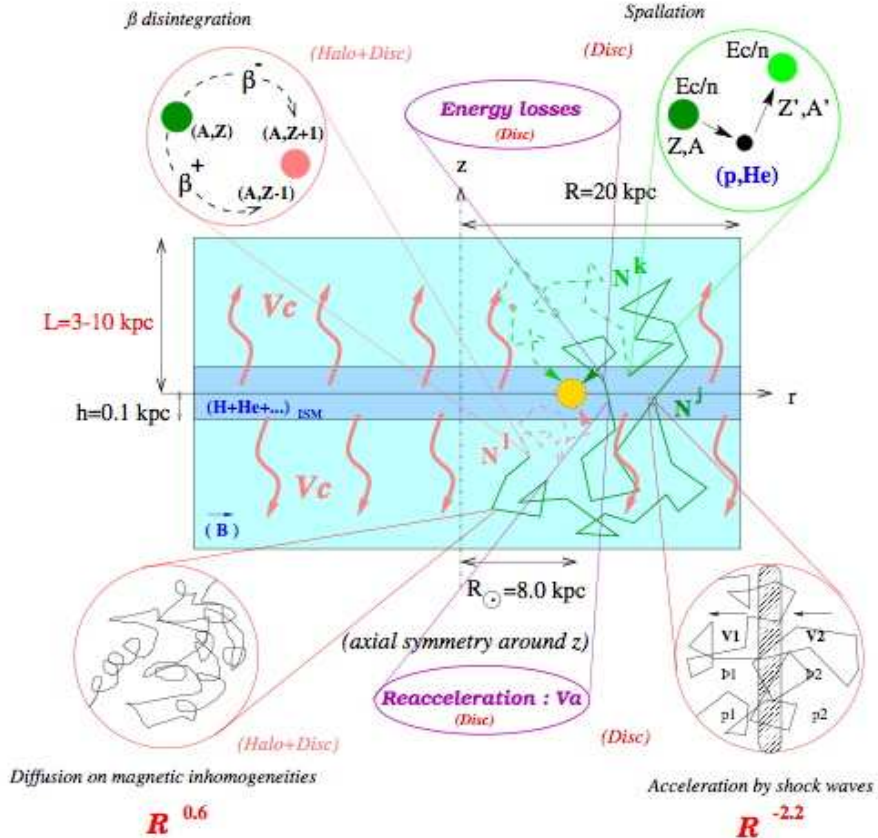


Fig. 1.1. Schematic edge-on view of the Milky Way diffusive halo (DH) as seen by a cosmic ray physicist. The stellar and gaseous disc is sandwiched between two thick layers which contain turbulent magnetic fields. After having been accelerated by SN driven shock waves or produced by DM species annihilating in the galactic halo, cosmic rays diffuse on magnetic inhomogeneities and are wiped away by a galactic wind with velocity V_C . They can lose energy and are also mildly subject to diffusive reacceleration. The former process is by far the dominant one in the case of electrons and positrons. This diagram has been borrowed from the review (44).

with a velocity $V_a \sim 20$ to 100 km s $^{-1}$, a second-order Fermi-mechanism is responsible for some mild diffusive reacceleration. Its coefficient K_{EE} depends on the particle velocity β and total energy E and is related to the space diffusion coefficient $K(E)$ through:

$$K_{EE} = \frac{2}{9} V_a^2 \frac{E^2 \beta^4}{K(E)} . \quad (1.3)$$

Finally, galactic convection wipes cosmic rays away from the disc with a velocity $V_C \sim 5$ to 15 km s $^{-1}$. We can assume steady state for the various populations of particles and write the master equation for the space and energy distribution function $\psi = dn/dE$ as (102):

$$\partial_z (V_C \psi) - K \Delta \psi + \partial_E \left\{ b^{\text{loss}}(E) \psi - K_{EE}(E) \partial_E \psi \right\} = q(\mathbf{x}, E) . \quad (1.4)$$

This equation applies to any charged species – nuclei, protons, antiprotons or positrons – as long as the rates for production q and energy loss $b^{\text{loss}}(E)$ are properly accounted for.

The solution of the master equation 1.4 has been deeply investigated and several different techniques lead to very similar fluxes at the Earth (78; 44). One possibility is a completely numerical solution. This is the way followed in the Galprop model (20; 58) which, thanks to a realistic gas distribution, can calculate gamma rays in addition to charged species(98). A completely different approach of the CRs transport through the DH relies on the calculation of the Green function of Eq. 1.4, which describes the probability for a CR that is produced at a location \vec{x} with energy E_S to be detected at the Earth with a degraded energy E . The Green function is then integrated over the diffusive volume (DH) and the energy range. This is *i.e.* the approach chosen to propagate positrons (19; 88; 87).

The Bessel expansion method, based on the cylindrical symmetry of the DH and on approximate values for the ISM (not relevant for charged CR propagation) permits a 2D fully analytical model. Numerical solution is required only for the diffusion in energy space. This is the model developed in (34; 44; 45; 41) and detailed more extensively in the following of this chapter. Very similar results for the propagation of stable primary and secondary nuclei have been obtained with the modified weighted slab technique (27).

According to this approach the region of the Galaxy inside which cosmic rays diffuse – the so-called diffusive halo (DH) – is pictured as a thick disc which matches the circular structure of the Milk Way as shown in Fig. 1.1. The galactic disc of stars and gas, where primary cosmic rays are accelerated, lies in the middle. It extends radially 20 kpc from the center and has a half-thickness h of 100 pc. Confinement layers where cosmic rays are trapped by diffusion lie above and beneath this thin disc of gas. The intergalactic medium starts at the vertical boundaries $z = \pm L$ as well as beyond a radius of $r = R \equiv 20$ kpc. The half-thickness L of the diffusive halo is not known and reasonable values range from 1 to 15 kpc. The diffusion coefficient K is the same everywhere whereas the convective velocity is exclusively vertical with component $V_C(z) = V_C \text{ sign}(z)$. This galactic wind, which is produced by the bulk of disc stars like the Sun, drifts away from its progenitors along

the vertical directions. The normalization coefficient K_0 , the index δ , the galactic drift velocity V_C and the Alfvén velocity V_a may be determined by studying the boron-to-carbon ratio (B/C) which is quite sensitive to cosmic ray transport and which may be used efficiently as a constraint.

The Bessel expansion method takes advantage of the axial symmetry of the DH and enforces a vanishing cosmic ray flux at a distance $R = 20$ kpc from the rotation axis of the Galaxy. This condition is actually implemented naturally by the following series expansion for ψ :

$$\psi(r, z, E) = \sum_{i=1}^{+\infty} P_i(z, E) J_0(\alpha_i r/R) . \quad (1.5)$$

The Bessel function of zeroth order J_0 vanishes at the points α_i . The radial dependence of ψ is now taken into account by the set of its Bessel transforms $P_i(z, E)$. The source term q may also be Bessel expanded into the corresponding functions $Q_i(z, E)$ so that the master equation (1.4) becomes

$$\begin{aligned} \partial_z (V_C P_i) - K \partial_z^2 P_i + K \left\{ \frac{\alpha_i}{R} \right\}^2 P_i + \\ + 2 h \delta(z) \partial_E \left\{ b^{\text{loss}}(E) P_i - K_{EE}(E) \partial_E P_i \right\} = Q_i(z, E) . \end{aligned} \quad (1.6)$$

Here, energy loss and diffusive reacceleration are confined inside the galactic disc – which is considered infinitely thin, hence the presence of an effective term $2 h \delta(z)$. The form of the source terms $Q_i(z, E)$ which appear in equation (1.6) depends on the nature of the cosmic ray particle.

1.3 Antiprotons in Cosmic Rays

In the case of antiprotons, the following mechanisms can in principle contribute to the source term in the transport equation 1.4:

- The spallation of high-energy primary nuclei impinging on the atoms of the interstellar medium inside the galactic disc produces secondary antiprotons.
- The annihilation of DM candidate particles throughout the Milky Way halo generates primary antiprotons. Notice that WIMP annihilations take place all over the diffusive halo.
- Tertiary antiprotons result from the inelastic and non-annihilating interactions with a nucleon at rest. The energy transfer may be sufficient to excite it as a Δ resonance. This mechanism redistributes antiprotons toward lower energies and flattens their spectrum (23). This yields the

source term:

$$q_{\bar{p}}^{\text{ter}}(r, E_{\bar{p}}) = \int_{E_{\bar{p}}}^{+\infty} \frac{d\sigma_{\bar{p}H \rightarrow \bar{p}X}}{dE_{\bar{p}}}(E'_{\bar{p}} \rightarrow E_{\bar{p}}) n_H \beta'_{\bar{p}} \psi_{\bar{p}}(r, E'_{\bar{p}}) dE'_{\bar{p}} - \sigma_{\bar{p}H \rightarrow \bar{p}X}(E_{\bar{p}}) n_H \beta_{\bar{p}} \psi_{\bar{p}}(r, E_{\bar{p}}) , \quad (1.7)$$

where the inelastic and non-annihilating differential cross section in this expression can be approximated by:

$$\frac{d\sigma_{\bar{p}H \rightarrow \bar{p}X}}{dE_{\bar{p}}} = \frac{\sigma_{\bar{p}H \rightarrow \bar{p}X}}{T'_{\bar{p}}} . \quad (1.8)$$

The initial antiproton kinetic energy is denoted by $T'_{\bar{p}}$. In order to take into account elastic scatterings on helium, one simply has to replace the hydrogen density by $n_H + 4^{2/3} n_{\text{He}}$.

- Antiprotons may also annihilate on interstellar H and He. This leads to a negative source term $-\Gamma_{\bar{p}}^{\text{ann}} \psi$, where the annihilation rate $\Gamma_{\bar{p}}^{\text{ann}}$ is defined as

$$\Gamma_{\bar{p}}^{\text{ann}} = \sigma_{\bar{p}H}^{\text{ann}} \beta_{\bar{p}} n_H + \sigma_{\bar{p}\text{He}}^{\text{ann}} \beta_{\bar{p}} n_{\text{He}} . \quad (1.9)$$

The annihilation cross section $\sigma_{\bar{p}H}^{\text{ann}}$ can be borrowed from (6; 7) and multiplied by a factor of $4^{2/3} \sim 2.5$, taking into account the higher geometric cross section, to get $\sigma_{\bar{p}\text{He}}^{\text{ann}}$. The average hydrogen n_H and helium n_{He} densities in the galactic disc are respectively set equal to 0.9 and 0.1 cm^{-3} .

1.3.1 Secondary antiprotons

Secondary antiprotons are produced by CR rays-spallation on the interstellar medium. They represent the background when searching for small contributions coming from exotic sources, like signals from DM annihilation.

The rate for the production of secondary antiprotons takes the following form:

$$q_{\bar{p}}^{\text{sec}}(r, E_{\bar{p}}) = \int_{E_{p,\alpha}^0}^{+\infty} n_{H,\alpha} \times \beta_{p,\alpha} \psi_{p,\alpha}(r, E_{p,\alpha}) \times dE_{p,\alpha} \times \frac{d\sigma}{dE_{\bar{p}}}(E_{p,\alpha} \rightarrow E_{\bar{p}}) , \quad (1.10)$$

for the interactions between cosmic ray protons and α particles, and hydrogen and helium nuclei in the interstellar medium (ISM).

Equation (1.4) may be solved according to the method outlined in Appendix B of (31) for an antiproton source located only in the galactic disk, as is the case for secondary antiprotons.

Some approximations may be at hand: in particular, setting the energy

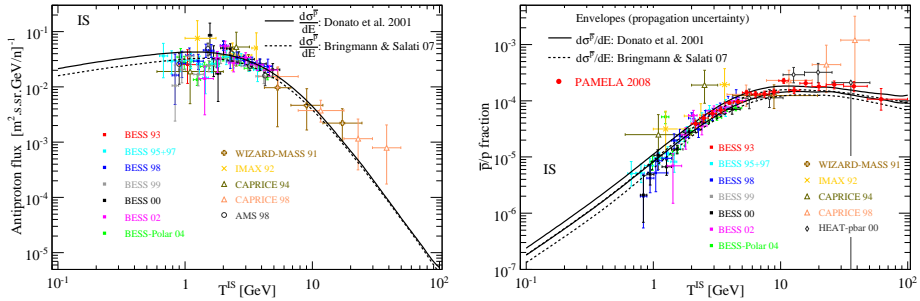


Fig. 1.2. Left panel: IS antiproton flux for the B/C best fit model and two parameterizations of the production cross section. Right panel: propagation uncertainty envelopes of the IS \bar{p}/p ratio for the same production cross sections as in the left panel. All data are demodulated using the force-field approximation: AMS 98 (37), IMAX 92 (13), CAPRICE 94 (15), WIZARD-MASS 91 (22), CAPRICE 98 (30), BESS93 (17), BESS 95+97 (28), BESS 98 (33), BESS 99 and 2000 (38), BESS 2002 (63), BESS Polar (79), WIZARD-MASS 1 (12), HEAT- \bar{p} (29), and PAMELA (80).

loss rate b^{loss} and the energy diffusion coefficient K_{EE} equal to zero does not affect sizeably the solution of the diffusion equation.

As for the the cosmic ray proton and helium fluxes, they can be borrowed from (31), where a fit to high energy (> 20 GeV/n) data is proposed. A more recent parameterization on IS fluxes has been derived in (91).

Once obtained the interstellar (IS) fluxes of antiprotons at the Sun's position in the Galaxy, we have to further propagate them inside the heliosphere, where the cosmic ray particles which eventually reach the Earth are affected by the presence of the solar wind. We model the effect of solar modulation by adopting the force field approximation of the full transport equation (9). In this model, the top-of-atmosphere (TOA) flux for a cosmic species Φ^{TOA} is obtained as:

$$\frac{\Phi^{\text{TOA}}(E^{\text{TOA}})}{\Phi^{\text{IS}}(E^{\text{IS}})} = \left(\frac{p^{\text{TOA}}}{p^{\text{IS}}} \right)^2 \quad (1.11)$$

where E and p denote the total energies and momenta of interstellar and TOA antiprotons, which are related by the energy shift:

$$E^{\text{TOA}} = E^{\text{IS}} - \phi \quad (1.12)$$

where the parameter ϕ is determined by fits on cosmic ray data. A value $\phi = 500$ MV is indicative of periods of minimal solar activity.

The secondary IS \bar{p} flux is displayed in the left panel of Fig. 1.2 along with the data demodulated according to the force-field prescription. We

Halo model	α	β	γ	$\rho_s [10^6 M_\odot \text{ kpc}^{-3}]$	$r_s [\text{kpc}]$
Cored isothermal (5)	2	2	0	7.90	4
NFW 97 (18)	1	3	1	5.38	21.75
Moore 04 (50)	1	3	1.16	2.54	32.62

Table 1.1. *Parameters in equation (1.15) for different halo models. The scale radius r_s and density ρ_s are strongly correlated with the virial mass of the Galaxy (32) and the values are borrowed from (55) for the Milky Way. When the DM distribution is cuspy ($\gamma \geq 1$) the divergence at the galactic center is smoothed according to the prescription of (75).*

either use the DTUNUC (31) \bar{p} production cross sections (solid line) or those discussed in Refs. (61; 75) (dashed line). The differences between the two curves illustrate the uncertainty related to the production cross sections, as emphasized in (31), where a careful and conservative analysis within the DTUNUC simulation settled a nuclear uncertainty of $\sim 25\%$ over the energy range $0.1 - 100$ GeV. The conclusion is similar here, although the two sets of cross sections differ mostly at low energy. In the right panel, along with the demodulated \bar{p}/p data, we show the curves bounding the propagation uncertainty on the \bar{p} calculation based either on the DTUNUC (31) \bar{p} production cross sections (solid lines) or those borrowed from (75) (dashed lines). The uncertainty arising from propagation is comparable to the nuclear one (31). The detailed calculation of that secondary component (43) has required the determination of the propagation–diffusion parameters that are consistent with the B/C data (35). By varying those parameters over the entire range allowed by the cosmic–ray nuclei measurements, the theoretical uncertainty on the antiproton secondary flux has been found to be 9% from 100 MeV to 1 GeV. It reaches a maximum of 24% at 10 GeV and decreases to 10% at 100 GeV.

From Fig. 1.2, it is manifest that the secondary contribution alone explains experimental data on the whole energetic range. It is not necessary to invoke an additional component to the standard astrophysical one.

1.3.2 Antiprotons from DM annihilation

The antiproton signal from annihilating DM particles leads to a primary component directly produced throughout the DH. The differential rate of production per unit volume and time is a function of space coordinates and

Case	δ	K_0 [kpc 2 /Myr]	L [kpc]	V_C [km/s]	V_a [km/s]
MIN	0.85	0.0016	1	13.5	22.4
MED	0.70	0.0112	4	12	52.9
MAX	0.46	0.0765	15	5	117.6

Table 1.2. *Typical combinations of diffusion parameters that are compatible with the B/C analysis (35). As shown in (51), these propagation models correspond respectively to minimal, medium and maximal primary antiproton fluxes.*

antiproton kinetic energy $T_{\bar{p}}$. It is defined as:

$$q_{\bar{p}}^{\text{DM}}(r, z, T_{\bar{p}}) = \xi^2 \langle \sigma_{\text{ann}} v \rangle g(T_{\bar{p}}) \left(\frac{\rho_{\chi}(r, z)}{m_{\chi}} \right)^2, \quad (1.13)$$

where $\langle \sigma_{\text{ann}} v \rangle$ denotes the average over the Galactic velocity distribution function of the WIMP pair annihilation cross section σ_{ann} multiplied by the relative velocity v . For a relic CDM particle able to explain the observed amount of cosmological dark matter (95; 97; 93) its value falls in the range $2 \div 3 \cdot 10^{-26}$ cm 3 s $^{-1}$ (unless special situations occurs, like dominant p-wave annihilation, dominant coannihilations or modified cosmology). For any DM candidate, σ_{ann} is nevertheless calculated from the model parameters. The WIMP mass is denoted by σ_{ann} and $\rho_{\chi}(r, z)$ is the mass distribution function of DM particles inside the Galactic halo. The quantity ξ parameterizes the fact that the dark halo may not be totally made of the species under scrutiny when this candidate possesses a relic abundance which does not allow it to be the dominant DM component (see e.g (85) or (10)). In this case $\xi < 1$. The quantity $g(T_{\bar{p}})$ in Eq. (1.13) denotes the antiproton differential spectrum per annihilation event, defined as:

$$\frac{dN_{\bar{p}}}{dE_{\bar{p}}} = \sum_{\text{F,h}} B_{\chi h}^{(\text{F})} \frac{dN_{\bar{p}}^h}{dE_{\bar{p}}}. \quad (1.14)$$

The annihilation into a quark or a gluon h is realized through the various final states F with branching ratios $B_{\chi h}^{(\text{F})}$. Quarks or gluons may in fact be directly produced when a WIMP pair annihilates or they may alternatively result from the intermediate production of Higgs bosons or gauge bosons. Each quark or gluon h then generates jets whose subsequent fragmentation and hadronization yield an antiproton energy spectrum $dN_{\bar{p}}^h/dE_{\bar{p}}$. The single production spectra are usually evaluated within Monte Carlo simulations of electroweak annihilation events (36). For details on the calculation of pure

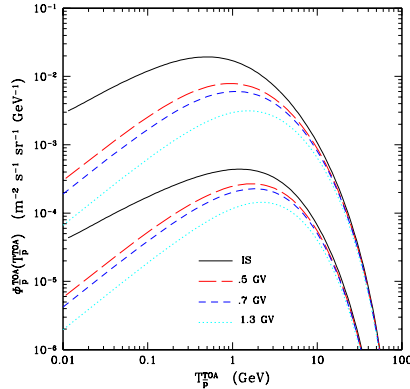


Fig. 1.3. Top-of-atmosphere antiproton fluxes as a function of the antiproton kinetic energy for the $m_\chi = 100$ GeV reference case. The upper (lower) set of curves refer to the maximal (minimal) set of astrophysical parameters. Solid curves show the interstellar fluxes. Broken curves show the effect of solar modulation at different periods of solar activity: $\phi = 500$ MV (long dashed), $\phi = 700$ MV (short dashed), $\phi = 1300$ MV (dotted).

state $dN_{\bar{p}}^h/dE_{\bar{p}}$ and of $g(T_{\bar{p}})$ in a Minimal Supersymmetric extension of the Standard Model (MSSM), see the Appendix of Ref. (51).

The distribution of DM inside galaxies is a very debated issue. Different analyses of rotational curves observed for several types of galaxies strongly favour a cored dark matter distribution, flattened towards the central regions (Ref. (53) and references therein). On the other side, many collisionless cosmological N-body simulations in Λ -CDM models are in good agreement among themselves (94), but for the very central regions some resolution issues remain open. It has been recently stressed that asymptotic slopes may not be reached at all at small scales (57; 73; 71; 66; 76). However, it is not clear whether the central cusp is steepened or flattened when the baryonic distribution is taken into account (e.g. (69; 70)). A detailed discussion may be found in Ref. (101; 99; 100). We wish to stress that the DM distribution is a crucial ingredient for the indirect signal into gamma-rays or neutrinos, while for antimatter it has been shown to be less relevant (51; 89), since antimatter diffuses and therefore the signal at Earth is more local, less dependent on the inner structure of the Galaxy as compared to gamma-rays and neutrinos.

To be definite, we will consider here a spherical DM galactic distribution

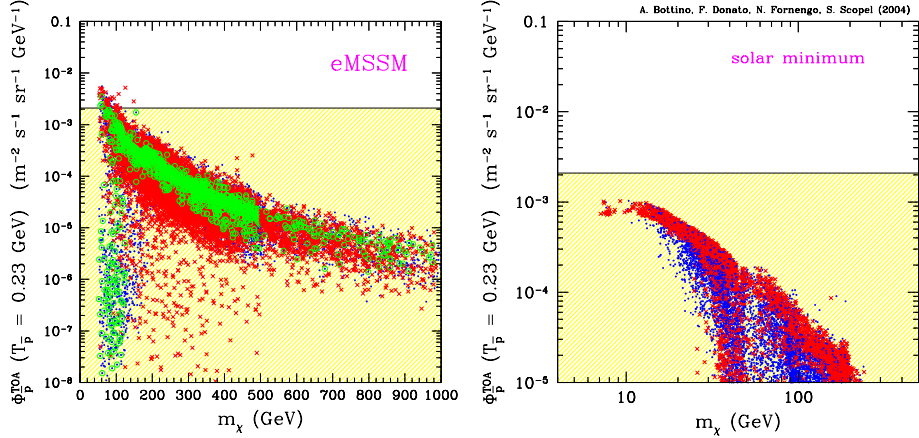


Fig. 1.4. LEFT: The scatter plot shows the antiproton flux at solar minimum from neutralino annihilation calculated at $T_{\bar{p}} = 0.23$ GeV, as a function of the neutralino mass for a generic scan of in a low-energy MSSM and for the MED set of astrophysical parameters (52). Crosses (in red) refer to cosmologically dominant neutralinos ($0.05 \leq \Omega_\chi h^2 \leq 0.3$); dots (in blue) refer to subdominant relic neutralinos ($\Omega_\chi h^2 < 0.05$). RIGHT: The same as in the left panel, but calculated for in scan of supersymmetric framework where gaugino non-universality is not assumed, and therefore lighter neutralinos are present (49). The astrophysical parameters are set at the MIN case, and solar modulation is at solar minimum.

with a dependence on galactocentric distance r parameterized by:

$$\rho(r) = \rho_s \left(\frac{r_s}{r} \right)^\gamma \left\{ 1 + \left(\frac{r}{r_s} \right)^\alpha \right\}^{(\gamma-\beta)/\alpha}. \quad (1.15)$$

The different profiles of Table 1.1 basically span the whole range of reasonable halo models with respect to indirect dark matter detection prospects.

The solution of the transport equation for a generic source term $q^{\text{prim}}(r, z, E)$ within Bessel expansion has been derived in (39):

$$\begin{aligned} N_i^{\bar{p}, \text{prim}}(z) &= \exp \left(\frac{V_c(|z| - L)}{2K} \right) \frac{y_i(L)}{A_i \sinh(S_i L/2)} \\ &\quad \left[\cosh(S_i z/2) + \frac{(V_c + 2h\Gamma_{\bar{p}}^{\text{ine}})}{KS_i A_i} \sinh(S_i z/2) \right] - \frac{y_i(z)}{KS_i} \end{aligned} \quad (1.16)$$

where:

$$y_i(z) = 2 \int_0^z \exp \left(\frac{V_c}{2K} (z - z') \right) \sinh \left(\frac{S_i}{2} (z - z') \right) q_i^{\text{prim}}(z') dz' \quad (1.17)$$

and the quantities S_i and A_i are defined as:

$$S_i \equiv \left\{ \frac{V_c^2}{K^2} + 4 \frac{\zeta_i^2}{R^2} \right\}^{1/2} \quad \text{and} \quad A_i(E) \equiv 2h \Gamma_{\bar{p}}^{ine} + V_c + K S_i \coth \left\{ \frac{S_i L}{2} \right\} . \quad (1.18)$$

In particular, at $z = 0$ where fluxes are measured, we have:

$$N_i^{\bar{p}, prim}(0) = \exp \left(\frac{-V_c L}{2K} \right) \frac{y_i(L)}{A_i \sinh(S_i L/2)} . \quad (1.19)$$

The three propagation models featured in Table 1.2 have been drawn from (51). The MED configuration provides the best fit to the B/C measurements whereas the MIN and MAX models point respectively to the minimal and maximal allowed antiproton fluxes which can be produced by WIMP annihilation.

Fig. 1.3 shows the TOA antiproton fluxes for a reference WIMP with $m_\chi = 100$ GeV, $2.3 \cdot 10^{-26}$ cm 3 s $^{-1}$, pure $\bar{b}b$ annihilation final state and for the maximal and minimal sets of astrophysical parameters. The variation of the astrophysical parameters induces a much larger uncertainty on the primary than on the secondary flux: in the first case, the uncertainty reaches two orders of magnitude for energies $T_{\bar{p}} \lesssim 1$ GeV, while in the second case it never exceeds 25%. The figure shows that solar modulation has the effect of depleting the low-energy tail of the antiproton flux. The effect is clearly more pronounced for periods of high solar activity, when the solar wind is stronger.

Predictions for antiprotons in various realization of supersymmetric theories have been performed (see. e.g. (52; 54; 49; 60; 65; 84)

. In Fig. 1.4 we show the predicted antiproton flux at kinetic energiy $T_{\bar{p}} = 0.23$ GeV, for two different supersymmetric models: the left panel (52) refers to a low-energy realization of the MSSM, while the right panel (52) stands for a scan of a supersymmetric scheme where gaugino non-universality is not assumed and therefore light neutralinos are present (48; 47). In both cases the shaded (yellow) region denotes the amount of antiprotons, in excess of the secondary component , which can be accommodated at $T_{\bar{p}} = 0.23$ GeV in order not to exceed the observed flux, as measured by BESS. All the points of the scatter plot that lie below the horizontal black line are therefore compatible with observations.

1.4 Antideuterons in Cosmic Rays

In the seminal Paper (26), it was proposed to look for cosmic antideuterons (\bar{D}) as a possible indirect signature for galactic dark matter. It was shown

that the antideuteron spectra deriving from DM annihilation is expected to be much flatter than the standard astrophysical component at low kinetic energies, $T_{\bar{d}} \lesssim 2\text{-}3 \text{ GeV/n}$. This argument motivated the proposal of a new space-borne experiment (46; 56; 67) looking for cosmic antimatter (antiproton and antideuteron) and having the potential to discriminate between standard and exotic components for a wide range of DM models. The present experimental upper limit (62) is still far from the expectations on the secondary antideuteron flux which are produced by spallation of cosmic rays on the interstellar medium (16; 61), but perspectives for the near future are very encouraging.

Once the astrophysical framework for the transport of (anti)nuclei is set, the calculation of the antideuteron flux rests on the \bar{D} specificities regarding the source term (i.e. primary or secondary) and its nuclear interactions [r.h.s. of Eq. (1.4)]. The tertiary term (see Eq. 1.7) requires specific inelastic non-annihilating cross sections which are detailed in the Appendix of Ref. (90).

The production of cosmic antideuterons is based on the fusion process of a \bar{p} and \bar{n} pair. One of the simplest but powerful treatment of the fusion of two or more nucleons is based on the so-called coalescence model which, despite its simplicity, is able to reproduce remarkably well the available data on light nuclei and antinuclei production in different kinds of collisions. In the coalescence model, the momentum distribution of the (anti)deuteron is proportional to the product of the (anti)proton and (anti)neutron momentum distribution (1; 2). That function depends on the difference $\Delta_{\vec{k}}$ between (anti)nucleon momenta. It is strongly peaked around $\Delta_{\vec{k}} \simeq \vec{0}$ (compare the minimum energy to form a \bar{D} , i.e. $4m_p$, with the binding energy $\sim 2.2 \text{ MeV}$), so that

$$\vec{k}_{\bar{p}} \simeq \vec{k}_{\bar{n}} \simeq \frac{\vec{k}_{\bar{D}}}{2}. \quad (1.20)$$

The \bar{D} density in momentum space is thus written as the \bar{p} density times the probability to find an \bar{n} within a sphere of radius p_0 around $\vec{k}_{\bar{p}}$ (see, e.g. Ref. (11)):

$$\gamma \frac{d\mathcal{N}_{\bar{D}}}{d\vec{k}_{\bar{D}}} = \frac{4\pi}{3} p_0^3 \cdot \gamma \frac{d\mathcal{N}_{\bar{p}}}{d\vec{k}_{\bar{p}}} \cdot \gamma \frac{d\mathcal{N}_{\bar{n}}}{d\vec{k}_{\bar{n}}}. \quad (1.21)$$

The coalescence momentum p_0 is a free parameter constrained by data on hadronic production In (61), a large set of data is used, including many pA reactions (see their Tab. I and references therein). This leads to an estimate of $p_0 = 79 \text{ MeV}$. At LEP energies, (anti)deuteron production occurs through e^+e^- annihilations into $q\bar{q}$ pairs, an electroweak mechanism similar to the \bar{D}

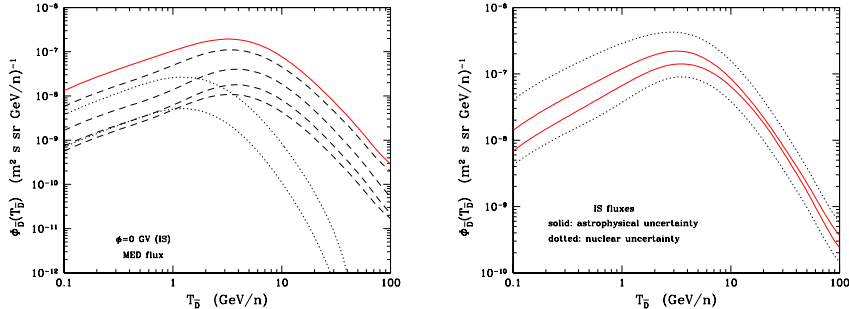


Fig. 1.5. Left panel: Contribution of all nuclear channels to the \bar{D} secondary flux. Dashed lines, from top to bottom refer to: $p+H$, $p+He$, $He+H$, $He+He$. Dotted lines, from top to bottom stand for: $\bar{p}+H$, $\bar{p}+He$. Solid line: sum of all the components. Right panel: Dominant uncertainties on the interstellar secondary \bar{D} flux. Solid lines: propagation uncertainty band. Dotted lines: nuclear uncertainty band.

production in DM annihilation reactions. Based on theoretical arguments, it has been argued (11) that the antideuteron yields in e^+e^- reactions should be smaller than in hadronic reactions. However, the ALEPH Collaboration (72) has found that this theoretical prediction (see Fig. 5 in ALEPH paper) underestimates their measured \bar{D} inclusive cross section. They derive (see their Fig. 6) a value $B_2 = 3.3 \pm 0.4 \pm 0.1 \times 10^{-3} \text{ GeV}^2$ at the Z resonance, which translates into $p_0 = 71.8 \pm 3.6 \text{ MeV}$, very close to the $p_0 = 79 \text{ MeV}$ derived for the hadronic production. From a rough estimate of the fusion process, one can estimate that the antideuteron fluxes are a factor of 10^4 lower than the antiproton ones. We will see in the following, and by comparing the results of the previous Section, that this result is recovered for both the primary and the secondary \bar{D} fluxes at Earth.

1.4.1 Secondary Antideuterons

The secondary \bar{D} flux is the sum of the six contributions corresponding to p , He and \bar{p} cosmic ray fluxes impinging on H and He IS gas (other reactions are negligible (61)). Contributions to the \bar{D} flux from $\bar{p} + H$ and $\bar{p} + He$ reactions are evaluated using the \bar{p} flux calculated in the same run. The production cross sections for these specific processes are those given in Ref. (61). The solution to the propagation equation has the same expression as for secondary antiprotons (92).

The different contributions to the total secondary antideuteron flux, calculated for the best fit propagation configuration (the “MED” one in Table

1.2), are shown in the left panel of Fig. 1.5. As expected, the dominant production channel is the one from p -H collisions, followed by the one from cosmic protons on IS helium (p-He). As shown in Ref. (61), the \bar{p} +H channel is dominant at low energies, and negligible beyond a few GeV/n. The effect of energy losses, reacceleration and tertiaries add up to replenish the low energy tail. The maximum of the total flux reaches the value of $2 \cdot 10^{-7}$ particles $(\text{m}^2 \text{ s sr GeV/n})^{-1}$ at 3-4 GeV/n. At 100 MeV/n it is decreased by an order of magnitude, thus preserving an interesting window for possible exotic contributions characterized by a flatter spectrum (see next Section).

For the determination of the propagation uncertainties, one can calculate the secondary antideuteron flux for all the propagation parameter combinations providing an acceptable fit to stable nuclei (35). The resulting envelope for the secondary antideuteron flux is presented in Fig. 1.5-left. The solid lines delimit the uncertainty band due to the degeneracy of the propagation parameters: at energies below 1–2 GeV/n, the uncertainty is 40–50 % around the average flux, while at 10 GeV/n it decreases to ~ 15 %. This behavior is analogous to that obtained for \bar{p} (31) and is easily understood. The degenerate transport parameters combine to give the same grammage in order to reproduce the B/C ratio. Indeed, the grammage crossed by C to produce the secondary species B is also crossed by p and He to produce the secondary \bar{p} and \bar{D} . In short, a similar propagation history associated with a well constrained B/C ratio explains the small uncertainty. The possible nuclear uncertainty can arise from two different sources. The first one is directly related to the elementary production process $d\sigma_{\bar{p}}^R$ and has been estimated to be conservatively $\pm 50\%$ (90). Second, there is the uncertainty on the coalescence momentum p_0 . Using an independent model (i.e. different from the coalescence scheme) for \bar{D} production, Ref. (61) found that, conservatively, the \bar{D} background was certainly no more than twice the flux calculated with $p_0 = 79$ MeV. The dotted lines in Fig. 1.5, right panel, take into account the sum of all the possible uncertainties of nuclear source (90). At the lowest energies the flux is uncertain by almost one order of magnitude, at 100 GeV/n by a factor of 4.

1.4.2 Antideuterons from DM annihilation

The source term for primary \bar{D} has the same form as the one for primary antiprotons in Eq. 1.13 ($\bar{p} \rightarrow \bar{D}$). The production of antideuterons from the pair-annihilation of supersymmetric dark matter particles in the halo of our Galaxy was proposed in (26), and subsequently discussed in (59) also for universal extra-dimension, Kaluza-Klein and warped extra-dimension dark

matter models. In ref. (90) primary antideuterons in different supersymmetric scenarios have been calculated in the full 2D propagation model, with a thorough estimation of all the possible uncertainty sources. As previously discussed (see Sect. 1.4) the production of a \bar{D} relies on the availability of a $\bar{p} - \bar{n}$ pair in a single DM annihilation. As in Ref. (26), we assume that the probability to form an antiproton (or an antineutron) with momentum $\vec{k}_{\bar{p}}$ ($\vec{k}_{\bar{n}}$), is essentially isotropic:

$$\frac{dN_{\bar{p}}}{dE_{\bar{p}}}(\chi + \chi \rightarrow \bar{p} + \dots) = 4\pi k_{\bar{p}} E_{\bar{p}} \mathcal{F}_{\bar{p}}(\sqrt{s} = 2m, E_{\bar{p}}). \quad (1.22)$$

Applying the factorization–coalescence scheme discussed above leads to the antideuteron differential multiplicity

$$\frac{dN_{\bar{D}}}{dE_{\bar{D}}} = \left(\frac{4p_0^3}{3k_{\bar{D}}} \right) \cdot \left(\frac{m_{\bar{D}}}{m_{\bar{p}}} \right) \cdot \sum_{F,h} B_{\chi h}^{(F)} \left\{ \frac{dN_{\bar{p}}^h}{dE_{\bar{p}}} \left(E_{\bar{p}} = \frac{E_{\bar{D}}}{2} \right) \right\}^2. \quad (1.23)$$

We assume, as discussed in Sect. 1.4, that the same value of the coalescence momentum $p_0 = 79$ MeV holds as for hadronic reactions.

The solution to the diffusion equation is provided by Eq. 1.19 where the specific cross sections have been reviewed, for instance, in Ref. (90). In the left panel of Fig. 1.6 the secondary \bar{D} flux for the median configuration of Table 1.2 is plotted alongside the primary flux from $m_{\chi} = 50$ GeV, calculated for the maximal, median and minimal propagation scenarios. The present BESS upper limit on the (negative) antideuteron search (62) is at a level of $2 \cdot 10^{-4} (\text{m}^2 \text{ s sr GeV/n})^{-1}$. We also plot the estimated sensitivities of the gaseous antiparticle spectrometer GAPS on a long duration balloon flight (LDB) and an ultra-long duration balloon mission (ULDB) (56; 67; 96), and of AMS–02 for three years of data taking. The perspectives to explore a part of the region where DM annihilation are mostly expected (i.e. the low-energy tail) are very promising. If one of these experiments will measure at least 1 antideuteron, it will be a clear signal of an exotic contribution to the cosmic antideuterons.

The discrimination power between primary and secondary \bar{D} flux may be deduced from the right panel of Fig. 1.6. The ratio of the primary to total TOA \bar{D} flux is plotted as a function of the kinetic energy per nucleon, for the three representative propagation models and different WIMP masses (the annihilation cross section is again fixed at the reference value). This ratio keeps higher than 0.7 for $T_{\bar{D}} < 1$ GeV/n except for $m_{\chi} = 500$ GeV. For propagation models with $L \gtrsim 4$ kpc – which is a very reasonable expectation – this ratio is at least 0.9 for masses below 100 GeV. Increasing the WIMP

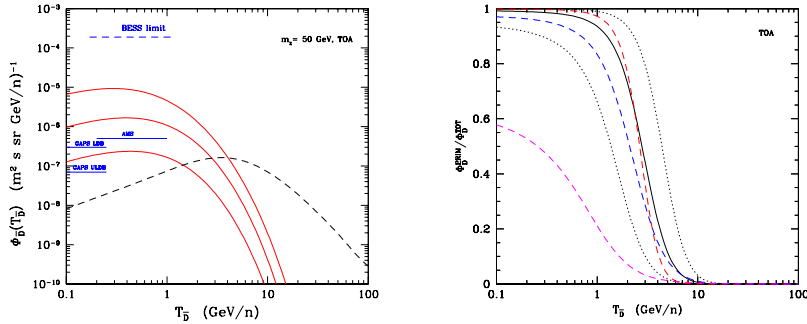


Fig. 1.6. Left panel: TOA primary (red solid lines) and secondary (black dashed line) antideuteron fluxes, modulated at solar minimum. The signal is derived for a $m_\chi = 50$ GeV WIMP and for the three propagation models of Table 1.2. The secondary flux is shown for the median propagation model. The upper dashed horizontal line shows the current BESS upper limit on the search for cosmic antideuterons. The three horizontal solid (blue) lines are the estimated sensitivities for (from top to bottom): AMS-02, GAPS on a long (LDB) and ultra-long (ULDB) duration balloon flights (56; 67; 96). Right panel: Ratio of the primary to total (signal+background) TOA antideuteron flux. Solid (black) curve refers to a WIMP mass of $m_\chi = 50$ GeV and for the MED propagation parameters. Dotted (black) lines show the MAX (upper) and MIN (lower) cases. Dashed lines refer to the MED propagation parameters and different masses, which are (from top to bottom): $m_\chi = 10, 100, 500$ GeV (red, blue, magenta respectively).

mass, we must descend to lower energies in order to maximize the primary-to-secondary ratio. However, for a $m_\chi = 500$ GeV WIMP we still have a 50-60% of DM contribution in the 0.1-0.5 GeV/n range. Of course, the evaluation of the theoretical uncertainties presented in this Paper must be kept in mind while confronting to real data. Fig. 1.6 clearly states that the antideuteron indirect DM detection technique is probably the most powerful one for low and intermediate WIMP-mass haloes.

The uncertainties due to propagation are similar to the ones quoted for primary antiprotons (90). At the lowest energies of hundreds of MeV/n the total uncertainty reaches almost 2 orders of magnitude, while at energies above 1 GeV/n it is about a factor of 30.

Examples for theoretical calculations for neutralino dark matter are shown in Fig. 1.7, where the reaching capabilities of the GAPS detector are derived and shown in terms of the neutralino annihilation parameters. The shaded

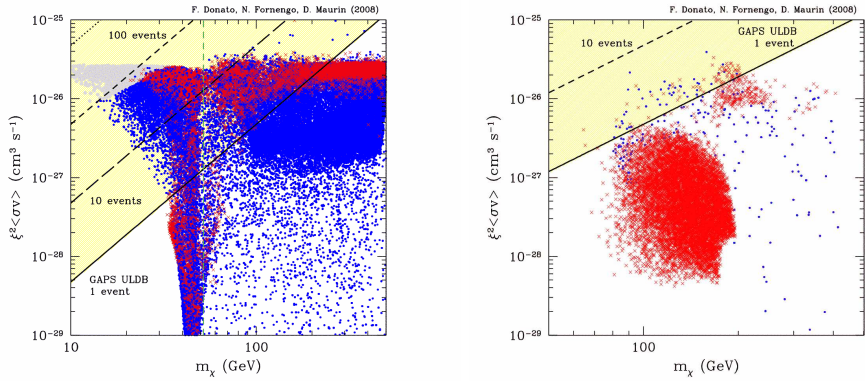


Fig. 1.7. LEFT: GAPS Ultra Long Duration Flight (ULDF) reach compared to predictions for neutralino dark matter in low-energy supersymmetric models, shown in the plane effective annihilation cross section $\xi^2 \langle \sigma_{\text{ann}} v \rangle_0$ vs. neutralino mass m_χ (90). The solid, long-dashed and short-dashed lines show our estimate for the capability of GAPS ULDB of measuring 1, 10 and 100 events, respectively, for the MED propagation model. The scatter plot reports the quantity $\xi^2 \langle \sigma_{\text{ann}} v \rangle_0$ calculated in a low-energy MSSM (for masses above the vertical [green] dashed line) and in non-universal gaugino models which predict low-mass neutralinos (47; 48). [Red] Crosses refer to cosmologically dominant neutralinos, while [blue] dots stand for subdominant neutralinos. Grey point are excluded by antiproton searches. RIGHT: The same as in the left panel, but for SUGRA scheme with non-universality in the higgs sector (90).

band denotes the region which will be covered by GAPS with a Ultra Long Duration Flight: sensitivity to neutralinos from a mass of a few GeV up to few hundreds of GeV is at hand and it will cover a large portion of the supersymmetric parameter space for models with gaugino non-universality (47; 48) or low-energy MSSM (90).

1.5 Positrons in Cosmic Rays

In the case of positrons and electrons, the master equation (1.4) describing the propagation of cosmic rays throughout the DH is dominated by space diffusion and energy losses. Above a few GeV, synchrotron radiation in the galactic magnetic fields as well as inverse Compton scattering on stellar light and on CMB photons dominate, hence the positron loss rate

$$b^{\text{loss}}(E) = \langle \dot{E} \rangle = - \frac{E^2}{E_0 \tau_E} . \quad (1.24)$$

The energy of reference E_0 is set equal to 1 GeV while the typical energy loss time τ_E is of order 10^{16} s. The master equation for positron propagation simplifies into

$$- K \Delta \psi + \partial_E \left\{ b^{\text{loss}}(E) \psi \right\} = q(\mathbf{x}, E) . \quad (1.25)$$

Above a few MeV, positrons are ultra-relativistic and the rigidity \mathcal{R} is proportional to the energy E . The space diffusion coefficient boils down to $K(\epsilon) = K_0 \epsilon^\delta$ where $\epsilon = E/E_0$. The solution of equation (1.25) proposed by (3; 21) is based on replacing the energy E by the pseudo-time

$$\tilde{t}(E) = \tau_E \left\{ v(E) = \frac{\epsilon^{\delta-1}}{1-\delta} \right\} , \quad (1.26)$$

and leads to the well-known heat equation

$$\frac{\partial \tilde{\psi}}{\partial \tilde{t}} - K_0 \Delta \tilde{\psi} = \tilde{q}(\mathbf{x}, \tilde{t}) , \quad (1.27)$$

where the space and energy positron density is now given by $\tilde{\psi} = \epsilon^2 \psi$ whereas the positron production rate has become $\tilde{q} = \epsilon^{2-\delta} q$. Because ϵ is dimensionless, both $\tilde{\psi}$ and \tilde{q} have the same dimensions as before. In this formalism, the energy losses which positrons experience are described by an evolution of their density with respect to the pseudo-time \tilde{t} . Equipped with these notations, we can write the cosmic ray positron density as the convolution

$$\psi_{e+}(\mathbf{x}, E) = \int_{E_S=E}^{E_S=+\infty} dE_S \int_{\text{DH}} d^3 \mathbf{x}_S G_{e+}(\mathbf{x}, E \leftarrow \mathbf{x}_S, E_S) q_{e+}(\mathbf{x}_S, E_S) . \quad (1.28)$$

The positron propagator $G_{e+}(\mathbf{x}, E \leftarrow \mathbf{x}_S, E_S)$ is defined as the probability for a particle injected at \mathbf{x}_S with the energy E_S to reach the location \mathbf{x} with the degraded energy $E \leq E_S$. It is proportional to the Green function \tilde{G} of the heat equation (1.27) through

$$G_{e+}(\mathbf{x}, E \leftarrow \mathbf{x}_S, E_S) = \frac{\tau_E}{E_0 \epsilon^2} \tilde{G}(\mathbf{x}, \tilde{t} \leftarrow \mathbf{x}_S, \tilde{t}_S) , \quad (1.29)$$

where the connection between the energy E and pseudo-time \tilde{t} is given by relation (1.26).

To build up our intuition, it is useful to derive the heat Green function \tilde{G} connecting a source at \mathbf{x}_S to the Earth in the simple case of an infinite DH. In this limit, there are no vertical boundaries and we get the Gaussian distribution

$$\tilde{G}(\mathbf{x}_\odot, \tilde{t} \leftarrow \mathbf{x}_S, \tilde{t}_S) = \left\{ \frac{1}{4\pi K_0 \tilde{\tau}} \right\}^{3/2} \exp \left\{ - \frac{r_\oplus^2}{4K_0 \tilde{\tau}} \right\} , \quad (1.30)$$

where $\tilde{\tau} = \tilde{t} - \tilde{t}_S$ is the typical duration over which the positron energy decreases from E_S to E . That timescale also includes information on the diffusion process. The distance between the source at \mathbf{x}_S and the Earth is denoted by r_\oplus . The concept of positron horizon is based on the Gaussian distribution (1.30) which is roughly constant within a sphere of radius

$$\lambda_D = \sqrt{4K_0\tilde{\tau}} , \quad (1.31)$$

and decreases sharply outside. So does the positron Green function G_{e^+} . The positron sphere – whose center is at the Earth where the observer stands – delineates actually the region of the diffusive halo from which positrons predominantly originate. The typical diffusion length λ_D gauges how far particles produced at the energy E_S travel before being detected with the energy E . It encodes at the same time the energy loss process and the diffusion throughout the magnetic fields of the Galaxy. A rapid inspection of equation (1.26) shows that λ_D increases as the detected energy E decreases, except for energies E_S at the source very close to E . The positron sphere is indeed fairly small at high energies, say above ~ 100 GeV, whereas it spreads over several kiloparsecs below 10 GeV. In the case where $E_S = 100$ GeV for instance, λ_D exceeds 3 kpc below an energy E of ~ 8 GeV.

The diffusive halo inside which cosmic rays propagate before escaping into the intergalactic medium is actually finite and \tilde{G} should account for that effect. In spite of the boundaries at $r = R \equiv 20$ kpc, we can decide that cosmic ray diffusion is not limited along the radial direction and that it operates as if it took place inside an infinite horizontal slab with half-thickness L . Sources located beyond the galactic radius R are disregarded since the convolution (1.28) is performed only over the DH. Because their energy is rapidly degraded as they propagate, positrons are produced close to where they are observed. Neglecting the effect of radial boundaries on the propagator G_{e^+} turns out to be a fair approximation (88) because positrons do not originate from far away on average. The effects of the radial boundaries down at the Earth are not significant insofar as cosmic rays tend to leak above and beneath the diffusive halo at $z = \pm L$ instead of traveling a long distance along the galactic plane.

The infinite slab hypothesis allows the radial and vertical directions to be disentangled and to express the reduced propagator \tilde{G} as

$$\tilde{G}(\mathbf{x}, \tilde{t} \leftarrow \mathbf{x}_S, \tilde{t}_S) = \frac{1}{4\pi K_0 \tilde{\tau}} \exp \left\{ -\frac{r^2}{4K_0 \tilde{\tau}} \right\} \tilde{V}(z, \tilde{t} \leftarrow z_S, \tilde{t}_S) , \quad (1.32)$$

where the radial distance between the source at \mathbf{x}_S and the point \mathbf{x} of

observation is now defined as

$$r = \left\{ (x - x_S)^2 + (y - y_S)^2 \right\}^{1/2}. \quad (1.33)$$

Should the half-thickness L be very large, expression (1.32) would boil down to the Gaussian distribution (1.30) and the vertical propagator \tilde{V} would be given by the 1D solution \mathcal{V}_{1D} of the heat equation (1.27)

$$\tilde{V}(z, \tilde{t} \leftarrow z_S, \tilde{t}_S) \equiv \mathcal{V}_{1D}(z, \tilde{t} \leftarrow z_S, \tilde{t}_S) = \frac{1}{\sqrt{4\pi K_0 \tilde{\tau}}} \exp \left\{ -\frac{(z - z_S)^2}{4K_0 \tilde{\tau}} \right\}. \quad (1.34)$$

But the diffusive halo has a finite vertical extent. We need to implement the corresponding boundary conditions and impose that the positron density vanishes at $z = \pm L$.

(i) A first approach relies on the method of the so-called electrical images and has been discussed in (21). Any point-like source inside the slab is associated to the infinite series of its multiple images through the boundaries at $z = \pm L$ which act as mirrors. The n -th image is located at

$$z_n = 2L n + (-1)^n z_S, \quad (1.35)$$

and has a positive or negative contribution depending on whether n is an even or odd number. When the diffusion time $\tilde{\tau}$ is small, the 1D solution (1.34) is a quite good approximation. The relevant parameter is actually

$$\zeta = \frac{L^2}{4K_0 \tilde{\tau}} \equiv \frac{L^2}{\lambda_D^2}, \quad (1.36)$$

and in the regime where it is much larger than 1, the propagation is insensitive to the vertical boundaries. On the contrary, when ζ is much smaller than 1, a large number of images need to be taken into account in the sum

$$\tilde{V}(z, \tilde{t} \leftarrow z_S, \tilde{t}_S) = \sum_{n=-\infty}^{+\infty} (-1)^n \mathcal{V}_{1D}(z, \tilde{t} \leftarrow z_n, \tilde{t}_S), \quad (1.37)$$

and convergence may be a problem.

(ii) It is fortunate that a quite different approach is possible in that case. The 1D diffusion equation (1.27) actually looks like the Schrödinger equation – though in imaginary time – that accounts for the behaviour of a particle inside an infinitely deep 1D potential well which extends from $z = -L$ to $z = +L$. The eigenfunctions of the associated Hamiltonian are both even

$$\varphi_n(z) = \sin \{k_n(L - |z|)\} \quad (1.38)$$

and odd

$$\varphi'_n(z) = \sin \{k'_n(L-z)\} \quad (1.39)$$

functions of the vertical coordinate z . The wave-vectors k_n and k'_n are respectively defined as

$$k_n = \left(n - \frac{1}{2}\right) \frac{\pi}{L} \text{ (even)} \quad \text{and} \quad k'_n = n \frac{\pi}{L} \text{ (odd)} . \quad (1.40)$$

The vertical propagator may be expanded as the series

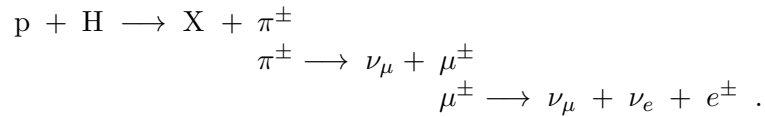
$$\tilde{V}(z, \tilde{t} \leftarrow z_S, \tilde{t}_S) = \sum_{n=1}^{+\infty} \frac{1}{L} \left\{ e^{-\lambda_n \tilde{\tau}} \varphi_n(z_S) \varphi_n(z) + e^{-\lambda'_n \tilde{\tau}} \varphi'_n(z_S) \varphi'_n(z) \right\} , \quad (1.41)$$

where the time constants λ_n and λ'_n are respectively equal to $K_0 k_n^2$ and $K_0 k'_n^2$. In the regime where ζ is much smaller than 1, for very large values of the diffusion time $\tilde{\tau}$, just a few eigenfunctions need to be considered in order for the sum (1.41) to converge. A close examination of these various expressions for \tilde{G} indicate that the energies E and E_S always come into play through the diffusion length λ_D so that the positron propagator may be written as

$$G_{e+}(\mathbf{x}, E \leftarrow \mathbf{x}_S, E_S) = \frac{\tau_E}{E_0 \epsilon^2} \tilde{G}(\mathbf{x} \leftarrow \mathbf{x}_S; \lambda_D) . \quad (1.42)$$

1.5.1 Secondary Positrons

Like for antiprotons, a background of secondary positrons is produced by the spallation of the interstellar medium by impinging high-energy particles. In that respect, the Milky Way looks like a giant accelerator where cosmic rays play the role of the beam whereas the galactic disc and its gas behave as the target. The dominant mechanism is the collision of protons with hydrogen atoms at rest producing charged pions π^\pm which decay into muons μ^\pm . The latter are also unstable and eventually lead to electrons and positrons through the chain



Below ~ 3 GeV, one of the protons is predominantly excited to a Δ resonance which subsequently decays into either a neutral or a charged pion. The former species produces gamma rays whereas the latter particle decays into positrons. Above ~ 7 GeV, pion production is well described in the framework of the scaling model. Various parameterizations are given in

the literature (4; 8) for the Lorentz invariant (LI) cross section $E_\pi d^3\sigma/d^3p_\pi$. Positrons may also be produced through kaons although this channel is rare. The positron production cross sections of these processes have been carefully computed in the appendices of (19). Notice also that useful parametric expressions for the yield and spectra of the stable secondary species produced in p-p collisions have been derived from experimental data and summarized in (68).

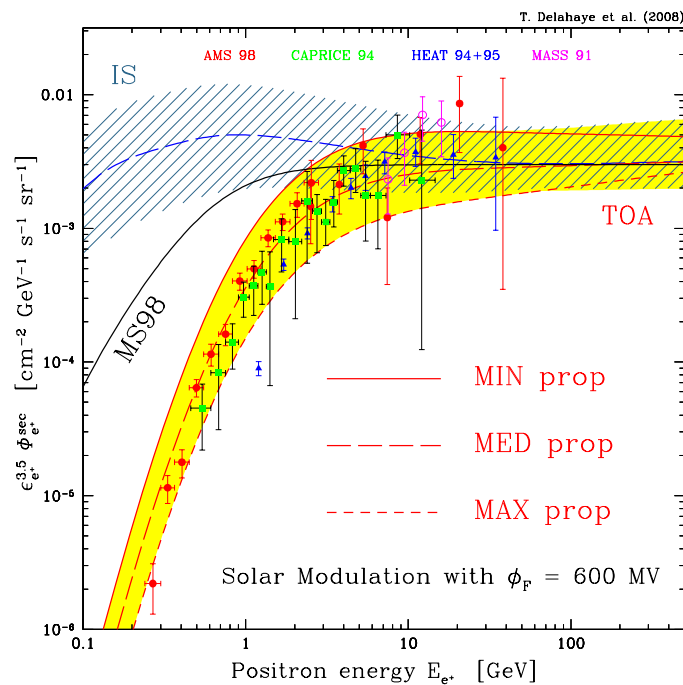


Fig. 1.8. Secondary positron flux as a function of the positron energy. The blue hatched band corresponds to the cosmic ray propagation uncertainty on the interstellar prediction whereas the yellow strip refers to the top-of-atmosphere fluxes. The long-dashed curves feature our reference model MED with a differential production cross section borrowed from (68) and the most recent measurements by BESS (77) of the cosmic ray proton and helium fluxes. The MIN, MED and MAX propagation parameters are displayed in table 1.2. The observations by CAPRICE (25) (green squares), HEAT (14) (blue triangles), MASS (42) (open circles) and AMS (24; 74) (red dots) are also indicated.

Cosmic ray protons with energy E_p induce a production of positrons per hydrogen atom with a rate

$$d\Gamma_{e^+}^{\text{sec}}(E_e) = \frac{d\sigma}{dE_e}(E_p \rightarrow E_e) \times \beta_p \times \{dn_p \equiv \psi_p(E_p) \times dE_p\} . \quad (1.43)$$

This leads to the source term

$$q_{e^+}^{\text{sec}}(\mathbf{x}, E_e) = 4\pi n_H(\mathbf{x}) \int \Phi_p(\mathbf{x}, E_p) \times dE_p \times \frac{d\sigma}{dE_e}(E_p \rightarrow E_e) . \quad (1.44)$$

That relation can be generalized in order to incorporate cosmic ray helium nuclei as well as interstellar helium. The gas of the galactic plane is generally assumed to be homogeneously spread. Because positrons detected at the Earth originate mostly from the solar neighborhood, we can safely disregard the space dependance of the proton and helium fluxes. Making use then of the measurements (31; 77) in relation (1.44), we can express the secondary positron flux as

$$\Phi_{e^+}^{\text{sec}}(\odot, \epsilon \equiv E_e/E_0) = \frac{\beta_{e^+}}{4\pi} \times \frac{\tau_E}{\epsilon^2} \times \int_{\epsilon}^{+\infty} d\epsilon_S \times \tilde{I}(\lambda_D) \times q_{e^+}^{\text{sec}}(\odot, \epsilon_S) . \quad (1.45)$$

The integral \tilde{I} is the convolution of the reduced positron Green function \tilde{G} over the galactic disc alone

$$\tilde{I}(\lambda_D) = \int_{\text{disc}} d^3 \mathbf{x}_S \tilde{G}(\mathbf{x}_\odot \leftarrow \mathbf{x}_S; \lambda_D) , \quad (1.46)$$

and depends only on λ_D as discussed above.

This method has been recently used (87) to derive the positron flux featured in figure 1.8. At 1 GeV, the width of the IS uncertainty strip corresponds to an increase by a factor of ~ 6 between the smallest and the largest positron fluxes allowed by the B/C constraint. That factor decreases down to 3.9 at 10 GeV and reaches 2.9 at 100 GeV. Once modulated with a Fisk potential ϕ_F of 600 MV, the blue hatched region is transformed into the yellow TOA band. Quite surprisingly, the MIN model (red solid curve) corresponds now to the **maximal** secondary positron flux whereas the MAX configuration (red short-dashed line) yields the **minimal** prediction. At fixed energies ϵ and ϵ_S , the smaller the diffusion coefficient K_0 , the smaller the diffusion length λ_D and the larger the integral (1.46). The latter reaches its maximal value of 1 whenever λ_D is smaller than the disc half-thickness h of 100 pc.

1.5.2 DM signals in Cosmic Positrons

An excess of the positron measurements with respect to the astrophysical background seems to appear above 10 GeV. This trend was present in the HEAT data (14) and has been recently nicely confirmed by the PAMELA

observations (82) of the positron fraction

$$\frac{e^+}{e^+ + e^-} \equiv \frac{\Phi_{e^+}^{\text{tot}}}{\Phi_{e^+}^{\text{tot}} + \Phi_{e^-}^{\text{tot}}} . \quad (1.47)$$

Different astrophysical contributions to the positron fraction in the 10 GeV region have already been explored in (14). More accurate and energy extended data will shed light on the effective presence of a bump in the positron absolute flux and on its physical interpretation. A possible explanation relies on DM species annihilating in the galactic halo (21; 64). This hypothesis has been strongly revived (86; 83) with the PAMELA observation of what seems a clear positron excess above 10 GeV.

Such an interpretation, though very exciting, is at some point limited by the uncertainties in the halo structure and in the cosmic ray propagation modeling. Equations (1.28) and (1.42) can be combined to yield the positron flux generated by the WIMP annihilations taking place within the Milky Way diffusive halo

$$\Phi_{e^+}^{\text{DM}}(\odot, \epsilon \equiv E_e/E_0) = \mathcal{F} \times \frac{\tau_E}{\epsilon^2} \times \int_{\epsilon}^{m_{\chi}/E_0} d\epsilon_S g(\epsilon_S) \tilde{I}_{\text{DM}}(\lambda_{\text{D}}) . \quad (1.48)$$

The information related to particle physics has been factored out in

$$\mathcal{F} = \frac{\beta}{4\pi} \xi^2 \langle \sigma_{\text{ann}} v \rangle \left\{ \frac{\rho_{\odot}}{m_{\chi}} \right\}^2 . \quad (1.49)$$

The energy distribution $g(\epsilon_S)$ describes the positron spectrum at the source and depends on the details of the WIMP annihilation mechanism. The halo integral \tilde{I}_{DM} is the convolution of the reduced positron propagator \tilde{G} with the square of the DM galactic density

$$\tilde{I}_{\text{DM}}(\lambda_{\text{D}}) = \int_{\text{DH}} d^3 \mathbf{x}_S \tilde{G}(\mathbf{x}_{\odot} \leftarrow \mathbf{x}_S; \lambda_{\text{D}}) \left\{ \frac{\rho_{\chi}(\mathbf{x}_S)}{\rho_{\odot}} \right\}^2 . \quad (1.50)$$

In figure 1.9, the positron fraction (1.47) is presented as a function of the positron energy E . The total positron flux at the Earth

$$\Phi_{e^+}^{\text{tot}} = \Phi_{e^+}^{\text{DM}} + \Phi_{e^+}^{\text{sec}} \quad (1.51)$$

encompasses the annihilation signal and a background component for which the results of (19) as parameterized by (21) have been used – see the brown thin solid lines. The mass of the DM species is 100 GeV and a NFW profile has been assumed. The observations featured in the various panels are indications of a possible excess of the positron fraction for energies above 10 GeV. Those measurements may be compared to the red thick solid curves

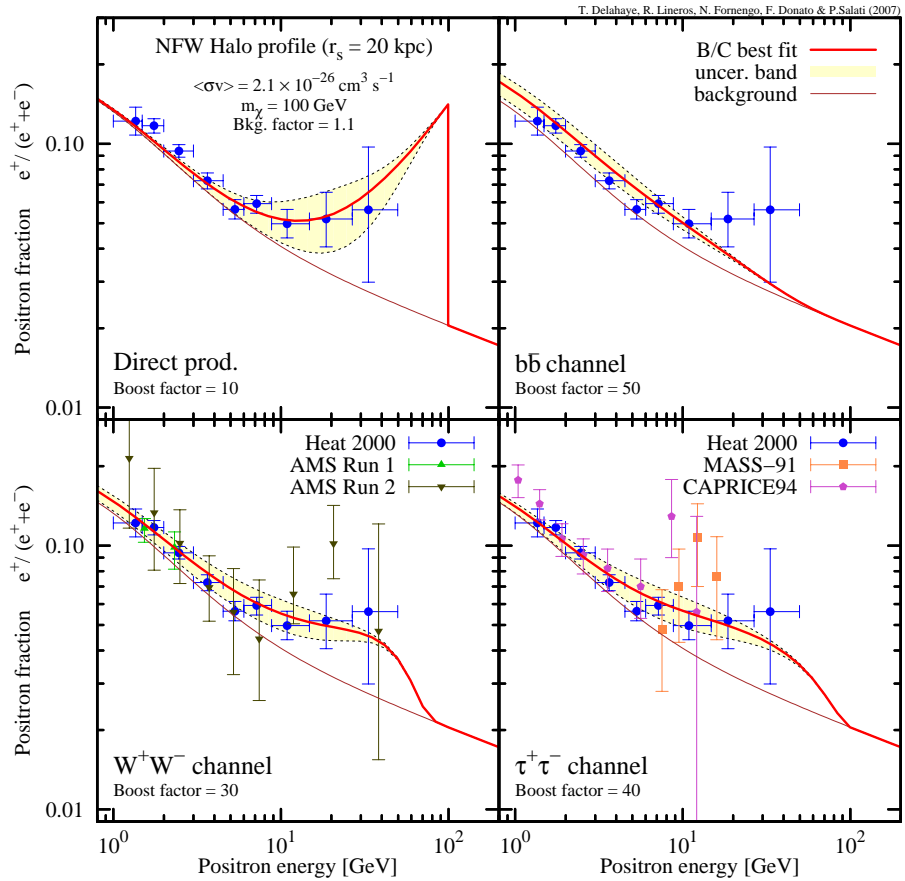


Fig. 1.9. The positron fraction $e^+/(e^- + e^+)$ is plotted versus the positron energy E for a 100 GeV WIMP in the case of a NFW DM profile. The four panels refer to different annihilation final states : direct e^+e^- production (top left), $b\bar{b}$ (top right), W^+W^- (bottom left) and $\tau^+\tau^-$ (bottom right). In each panel, the brown thin solid line stands for the positron background borrowed from (19) and parameterized by (21). The red thick solid curve refers to the **total** positron flux where the signal is propagated with the best-fit choice of the astrophysical parameters, *i.e.* the configuration MED of table 1.2. The yellow area features the total uncertainty band arising from cosmic ray propagation. The different models found in (35) to be compatible with the B/C ratio all yield a positron fraction which is enclosed inside this yellow strip. Experimental data from HEAT (14), AMS (24; 74), CAPRICE (25) and MASS (42) are also presented for comparison. Figure from (88).

that correspond to the MED configuration of table 1.2. In order to get a reasonable agreement between the DM predictions and the data, the annihilation signal has been boosted by an energy-independent factor ranging from 10 to 50 as indicated in each panel. As is clear in the upper left panel,

the case of direct production offers a very good agreement with the positron excess. Notice how well all the data points lie within the yellow uncertainty band. A boost factor of 10 is enough to obtain an excellent agreement between the measurements and the median flux. A smaller value would be required for a flux at the upper envelope of the uncertainty strip. The W^+W^- and $\tau^+\tau^-$ channels may also reproduce reasonably well the observations, especially once the uncertainty arising from cosmic ray propagation throughout the Milky Way diffusive halo is taken into account. They need though larger boost factors of the order of 30 to 40. On the contrary, softer production channels, like the $b\bar{b}$ case, are unable to match the features of the positron bump.

1.6 Conclusions

Crucial information on the astronomical dark matter pervading the Galaxy will be provided by crossing the positron (82) and antiproton (81) observations. An excess seems to be present in the positron flux but does not show up in the antiproton signal. This may lead to strong constraints on the properties of the DM species as mentioned for instance in (86; 91). Pure leptonic models are a priori favored since even a small branching ratio to quarks or gauge bosons would translate into an overproduction of antiprotons which is not seen. Some attention needs to be paid though insofar as antiprotons could be rehabilitated depending on how cosmic ray transport is modeled. The forthcoming measurements will be crucial to ascertain the presence of WIMPs in outer space and to study their nature.

Bibliography

- [1] S. T. Butler and C. A. Pearson. Deuterons from High-Energy Proton Bombardment of Matter. *Physical Review*, 129:836–842, January 1963.
- [2] A. Schwarzschild and Č. Zupančič. Production of Tritons, Deuterons, Nucleons, and Mesons by 30-GeV Protons on A1, Be, and Fe Targets. *Physical Review*, 129:854–862, January 1963.
- [3] S. V. Bulanov and V. A. Dogel. The Influence of the Energy Dependence of the Diffusion Coefficient on the Spectrum of the Electron Component of Cosmic Rays and the Radio Background Radiation of the Galaxy. *Ap&SS*, 29:305–318, August 1974.
- [4] G. D. Badhwar, R. L. Golden, and S. A. Stephens. Analytic representation of the proton-proton and proton-nucleus cross-sections and its application to the sea-level spectrum and charge ratio of muons. *Phys. Rev. D*, 15:820–831, February 1977.
- [5] John N. Bahcall and R. M. Soneira. The Universe at faint magnetitudes. 2. Models for the predicted star counts. *Astrophys. J. Suppl.*, 44:73–110, 1980.
- [6] L. C. Tan and L. K. Ng. PARAMETRIZATION OF ANTI-P INVARIANT CROSS-SECTION IN P P COLLISIONS USING A NEW SCALING VARIABLE. *Phys. Rev.*, D26:1179–1182, 1982.
- [7] L. C. Tan and L. K. Ng. Calculation of the equilibrium antiproton spectrum. *Journal of Physics G Nuclear Physics*, 9:227–242, 1983.
- [8] L. C. Tan and L. K. Ng. PARAMETRIZATION OF HADRON INCLUSIVE CROSS-SECTIONS IN P P COLLISIONS EXTENDED TO VERY LOW-ENERGIES. *J. Phys.*, G9:1289–1308, 1983.
- [9] J. S. Perko. Solar modulation of galactic antiprotons. *A&A*, 184:119–121, October 1987.
- [10] A. Bottino, V. de Alfaro, N. Fornengo, G. Mignola, and S. Scopel.

A New investigation about neutralino dark matter: Relic density and detection rates. *Astropart. Phys.*, 1:61–76, 1992.

[11] G. Gustafson and J. Hakkinen. Deuteron production in e+ e- annihilation. *Z. Phys.*, C61:683–688, 1994.

[12] M. Hof et al. Measurement of Cosmic-Ray Antiprotons from 3.7 to 19 GeV. *ApJ*, 467:L33, August 1996.

[13] J. W. Mitchell et al. Measurement of 0.25-3.2 GeV Antiprotons in the Cosmic Radiation. *Phys. Rev. Lett.*, 76:3057–3060, April 1996.

[14] S. W. Barwick, J. J. Beatty, A. Bhattacharyya, C. R. Bower, C. J. Chaput, S. Coutu, G. A. de Nolfo, J. Knapp, D. M. Lowder, S. McKee, D. Mueller, J. A. Musser, S. L. Nutter, E. Schneider, S. P. Swordy, G. Tarle, A. D. Tomasch, E. Torbet, and The HEAT Collaboration. Measurements of the Cosmic-Ray Positron Fraction from 1 to 50 GeV. *ApJ*, 482:L191+, June 1997.

[15] M. Boezio et al. The Cosmic-Ray Antiproton Flux between 0.62 and 3.19 G eV Measured Near Solar Minimum Activity. *ApJ*, 487:415–+, September 1997.

[16] P. Chardonnet, J. Orloff, and P. Salati. The production of anti-matter in our galaxy. *Phys. Lett. B*, 409:313–320, September 1997.

[17] A. Moiseev et al. Cosmic-Ray Antiproton Flux in the Energy Range from 200 to 600 MeV. *ApJ*, 474:479–+, January 1997.

[18] J. F. Navarro, C. S. Frenk, and S. D. M. White. A Universal Density Profile from Hierarchical Clustering. *ApJ*, 490:493, December 1997.

[19] I. V. Moskalenko and A. W. Strong. Production and Propagation of Cosmic-Ray Positrons and Electrons. *ApJ*, 493:694, January 1998.

[20] A. W. Strong and I. V. Moskalenko. Propagation of Cosmic-Ray Nucleons in the Galaxy. *ApJ*, 509:212–228, December 1998.

[21] Edward A. Baltz and Joakim Edsjo. Positron Propagation and Fluxes from Neutralino Annihilation in the Halo. *Phys. Rev.*, D59:023511, 1999.

[22] G. Basini et al. The Flux of Cosmic Ray Antiprotons from 3.7 to 24 GeV. *26th International Cosmic Ray Conference, Salt Lake City*, 3:77, August 1999.

[23] L. Bergström, J. Edsjo, and P. Ullio. Cosmic Antiprotons as a Probe for Supersymmetric Dark Matter? *ApJ*, 526:215–235, November 1999.

[24] J. Alcaraz et al. Leptons in near earth orbit. *Phys. Lett.*, B484:10–22, 2000.

[25] M. Boezio, P. Carlson, T. Francke, N. Weber, M. Suffert, M. Hof, W. Menn, M. Simon, S. A. Stephens, R. Bellotti, F. Cafagna, M. Castellano, M. Circella, C. De Marzo, N. Finetti, P. Papini,

S. Piccardi, P. Spillantini, M. Ricci, M. Casolino, M. P. De Pascale, A. Morselli, P. Picozza, R. Sparvoli, G. Barbiellini, U. Bravar, P. Schiavon, A. Vacchi, N. Zampa, C. Grimaldi, J. W. Mitchell, J. F. Ormes, R. E. Streitmatter, R. L. Golden, and S. J. Stochaj. The Cosmic-Ray Electron and Positron Spectra Measured at 1 AU during Solar Minimum Activity. *ApJ*, 532:653–669, March 2000.

[26] F. Donato, N. Fornengo, and P. Salati. Antideuterons as a signature of supersymmetric dark matter. *Phys. Rev. D*, 62(4):043003, August 2000.

[27] Frank C. Jones, Andrew Lukasiak, Vladimir Ptuskin, and William Webber. The Modified Weighted Slab Technique: Models and Results. 2000.

[28] S. Orito et al. Precision Measurement of Cosmic-Ray Antiproton Spectrum. *Phys. Rev. Lett.*, 84:1078–1081, February 2000.

[29] A. S. Beach et al. Measurement of the Cosmic-Ray Antiproton-to-Proton Abundance Ratio between 4 and 50 GeV. *Phys. Rev. Lett.*, 87(26):271101, December 2001.

[30] M. Boezio et al. The Cosmic-Ray Antiproton Flux between 3 and 49 GeV. *ApJ*, 561:787–799, November 2001.

[31] F. Donato, D. Maurin, P. Salati, A. Barrau, G. Boudoul, and R. Taillet. Antiprotons from Spallations of Cosmic Rays on Interstellar Matter. *ApJ*, 563:172–184, December 2001.

[32] V. R. Eke, J. F. Navarro, and M. Steinmetz. The Power Spectrum Dependence of Dark Matter Halo Concentrations. *ApJ*, 554:114–125, June 2001.

[33] T. Maeno et al. Successive measurements of cosmic-ray antiproton spectrum in a positive phase of the solar cycle. *Astropart. Phys.*, 16:121–128, November 2001.

[34] D. Maurin, F. Donato, R. Taillet, and P. Salati. Cosmic Rays below Z=30 in a diffusion model: new constraints on propagation parameters. *Astrophys. J.*, 555:585–596, 2001.

[35] D. Maurin, F. Donato, R. Taillet, and P. Salati. Cosmic Rays below Z=30 in a Diffusion Model: New Constraints on Propagation Parameters. *ApJ*, 555:585–596, July 2001.

[36] Torbjorn Sjostrand et al. High-energy-physics event generation with PYTHIA 6.1. *Comput. Phys. Commun.*, 135:238–259, 2001.

[37] M. Aguilar et al. The Alpha Magnetic Spectrometer (AMS) on the International Space Station: Part I - results from the test flight on the space shuttle. *Phys. Rep.*, 366:331–405, August 2002.

- [38] Y. Asaoka et al. Measurements of Cosmic-Ray Low-Energy Antiproton and Proton Spectra in a Transient Period of Solar Field Reversal. *Phys. Rev. Lett.*, 88(5):051101–+, February 2002.
- [39] A. Barrau, G. Boudoul, F. Donato, D. Maurin, P. Salati, and R. Taillet. Antiprotons from primordial black holes. *A&A*, 388:676–687, June 2002.
- [40] Fabien Casse, Martin Lemoine, and Guy Pelletier. Transport of cosmic rays in chaotic magnetic fields. *Phys. Rev.*, D65:023002, 2002.
- [41] Fiorenza Donato, David Maurin, and Richard Taillet. β -Radioactive Cosmic Rays in a diffusion model: test for a local bubble? *Astron. Astrophys.*, 381:539–559, 2002.
- [42] C. Grimaldi, S. A. Stephens, F. S. Cafagna, G. Basini, R. Bellotti, M. T. Brunetti, M. Circella, A. Codino, C. De Marzo, M. P. De Pascale, N. Finetti, R. L. Golden, M. Hof, W. Menn, J. W. Mitchell, A. Morselli, J. F. Ormes, P. Papini, C. Pfeifer, S. Piccardi, P. Picozza, M. Ricci, M. Simon, P. Spillantini, S. J. Stochaj, and R. E. Streitmatter. Measurements of the absolute energy spectra of cosmic-ray positrons and electrons above 7 GeV. *A&A*, 392:287–294, September 2002.
- [43] D. Maurin, R. Taillet, and F. Donato. New results on source and diffusion spectral features of Galactic cosmic rays: I B/C ratio. *A&A*, 394:1039–1056, November 2002.
- [44] David Maurin et al. Galactic cosmic ray nuclei as a tool for astroparticle physics. 2002.
- [45] David Maurin, Richard Taillet, and Fiorenza Donato. New results on source and diffusion spectral features of Galactic cosmic rays: I- B/C ratio. *Astron. Astrophys.*, 394:1039–1056, 2002.
- [46] K. Mori, C. J. Hailey, E. A. Baltz, W. W. Craig, M. Kamionkowski, W. T. Serber, and P. Ullio. A Novel Antimatter Detector Based on X-Ray Deexcitation of Exotic Atoms. *ApJ*, 566:604–616, February 2002.
- [47] A. Bottino, F. Donato, N. Fornengo, and S. Scopel. Lower bound on the neutralino mass from new data on CMB and implications for relic neutralinos. *Phys. Rev.*, D68:043506, 2003.
- [48] A. Bottino, N. Fornengo, and S. Scopel. Light relic neutralinos. *Phys. Rev.*, D67:063519, 2003.
- [49] A. Bottino, F. Donato, N. Fornengo, and S. Scopel. Indirect signals from light neutralinos in supersymmetric models without gaugino mass unification. *Phys. Rev.*, D70:015005, 2004.

- [50] J. Diemand, B. Moore, and J. Stadel. Convergence and scatter of cluster density profiles. *MNRAS*, 353:624–632, September 2004.
- [51] F. Donato, N. Fornengo, D. Maurin, P. Salati, and R. Taillet. Antiprotons in cosmic rays from neutralino annihilation. *Phys. Rev. D*, 69(6):063501, March 2004.
- [52] F. Donato, Nicolao Fornengo, D. Maurin, and P. Salati. Antiprotons in cosmic rays from neutralino annihilation. *Phys. Rev.*, D69:063501, 2004.
- [53] Fiorenza Donato and Paolo Salucci. Cores of Dark Matter Halos Correlate with Disk Scale Lengths. *Mon. Not. Roy. Astron. Soc.*, 353:L17–L22, 2004.
- [54] Joakim Edsjo, Mia Schelke, and Piero Ullio. Direct versus indirect detection in mSUGRA with self-consistent halo models. *JCAP*, 0409:004, 2004.
- [55] N. Fornengo, L. Pieri, and S. Scopel. Neutralino annihilation into gamma-rays in the Milky Way and in external galaxies. *Phys. Rev.*, D70:103529, 2004.
- [56] C. J. Hailey et al. Development of the gaseous antiparticle spectrometer for space-based antimatter detection. *Nuclear Instruments and Methods in Physics Research B*, 214:122–125, January 2004.
- [57] J. F. Navarro, E. Hayashi, C. Power, A. R. Jenkins, C. S. Frenk, S. D. M. White, V. Springel, J. Stadel, and T. R. Quinn. The inner structure of Λ CDM haloes - III. Universality and asymptotic slopes. *MNRAS*, 349:1039–1051, April 2004.
- [58] Andrew W. Strong, Igor V. Moskalenko, and Olaf Reimer. Diffuse Galactic continuum gamma rays. A model compatible with EGRET data and cosmic-ray measurements. *Astrophys. J.*, 613:962–976, 2004.
- [59] H. Baer and S. Profumo. Low energy antideuterons: shedding light on dark matter. *Journal of Cosmology and Astro-Particle Physics*, 12:8, December 2005.
- [60] Howard Baer, Azar Mustafayev, Stefano Profumo, Alexander Belyaev, and Xerxes Tata. Direct, indirect and collider detection of neutralino dark matter in SUSY models with non-universal Higgs masses. *JHEP*, 07:065, 2005.
- [61] R. Duperray et al. Flux of light antimatter nuclei near earth, induced by cosmic rays in the galaxy and in the atmosphere. *Phys. Rev.*, D71:083013, 2005.
- [62] H. Fuke, T. Maeno, K. Abe, S. Haino, Y. Makida, S. Matsuda, H. Matsumoto, J. W. Mitchell, A. A. Moiseev, J. Nishimura, M. Nozaki,

S. Orito, J. F. Ormes, M. Sasaki, E. S. Seo, Y. Shikaze, R. E. Streitmatter, J. Suzuki, K. Tanaka, K. Tanizaki, T. Yamagami, A. Yamamoto, Y. Yamamoto, K. Yamato, T. Yoshida, and K. Yoshimura. Search for Cosmic-Ray Antideuterons. *Phys. Rev. Lett.*, 95(8):081101, August 2005.

[63] S. Haino et al. Measurement of cosmic-ray antiproton spectrum with BESS-2002. 3:13–+, 2005.

[64] Dan Hooper and Joseph Silk. Searching for dark matter with future cosmic positron experiments. *Phys. Rev.*, D71:083503, 2005.

[65] Francesc Ferrer, Lawrence M. Krauss, and Stefano Profumo. Indirect detection of light neutralino dark matter in the NMSSM. *Phys. Rev.*, D74:115007, 2006.

[66] A. W. Graham, D. Merritt, B. Moore, J. Diemand, and B. Terzić. Empirical Models for Dark Matter Halos. II. Inner Profile Slopes, Dynamical Profiles. *Astron. J.*, 132:2701–2710, December 2006.

[67] C. J. Hailey, T. Aramaki, W. W. Craig, L. Fabris, F. Gahbauer, J. E. Koglin, N. Madden, K. Mori, H. T. Yu, and K. P. Ziack. Accelerator testing of the general antiparticle spectrometer; a novel approach to indirect dark matter detection. *Journal of Cosmology and Astroparticle Physics*, 1:7–+, January 2006.

[68] T. Kamae, N. Karlsson, T. Mizuno, T. Abe, and T. Koi. Parameterization of γ , $e^{+/-}$, and Neutrino Spectra Produced by p-p Interaction in Astronomical Environments. *ApJ*, 647:692–708, August 2006.

[69] A. V. Macciò, B. Moore, J. Stadel, and J. Diemand. Radial distribution and strong lensing statistics of satellite galaxies and substructure using high-resolution Λ CDM hydrodynamical simulations. *Mon. Not. Roy. Astron. Soc.*, 366:1529–1538, March 2006.

[70] Sergey Mashchenko, H. M. P. Couchman, and James Wadsley. Cosmological puzzle resolved by stellar feedback in high redshift galaxies. *Nature*, 442:539, 2006.

[71] D. Merritt, A. W. Graham, B. Moore, J. Diemand, and B. Terzić. Empirical Models for Dark Matter Halos. I. Nonparametric Construction of Density Profiles and Comparison with Parametric Models. *AJ*, 132:2685–2700, December 2006.

[72] S. et al. Schael. Deuteron and anti-deuteron production in e^+e^- collisions at the Z resonance. *Phys. Lett. B*, 639:192–201, August 2006.

[73] F. Stoehr. Circular velocity profiles of dark matter haloes. *Mon. Not. Roy. Astron. Soc.*, 365:147–152, January 2006.

[74] M. Aguilar et al. Cosmic-ray positron fraction measurement from 1-GeV to 30- GeV with AMS-01. *Phys. Lett.*, B646:145–154, 2007.

- [75] T. Bringmann and P. Salati. Galactic antiproton spectrum at high energies: Background expectation versus exotic contributions. *Phys. Rev. D*, 75(8):083006, April 2007.
- [76] M. Ricotti, A. Pontzen, and M. Viel. Is the Concentration of Dark Matter Halos at Virialization Universal? *Astrophys. J. Lett.*, 663:L53–L56, July 2007.
- [77] Y. Shikaze et al. Measurements of 0.2–20 GeV/n cosmic-ray proton and helium spectra from 1997 through 2002 with the BESS spectrometer. *Astropart. Phys.*, 28:154–167, September 2007.
- [78] Andrew W. Strong, Igor V. Moskalenko, and Vladimir S. Ptuskin. Cosmic-ray propagation and interactions in the Galaxy. *Ann. Rev. Nucl. Part. Sci.*, 57:285–327, 2007.
- [79] K. Abe et al. Measurement of cosmic-ray low-energy antiproton spectrum with the first BESS-Polar Antarctic flight. *ArXiv e-prints*, May 2008.
- [80] O. Adriani et al. A new measurement of the antiproton-to-proton flux ratio up to 100 GeV in the cosmic radiation. 2008.
- [81] O. Adriani et al. A new measurement of the antiproton-to-proton flux ratio up to 100 GeV in the cosmic radiation. 2008.
- [82] O. Adriani et al. Observation of an anomalous positron abundance in the cosmic radiation. 2008.
- [83] Lars Bergstrom, Torsten Bringmann, and Joakim Edsjo. New Positron Spectral Features from Supersymmetric Dark Matter - a Way to Explain the PAMELA Data? 2008.
- [84] A. Bottino, F. Donato, N. Fornengo, and S. Scopel. Interpreting the recent results on direct search for dark matter particles in terms of relic neutralino. *Phys. Rev.*, D78:083520, 2008.
- [85] A. Bottino, F. Donato, N. Fornengo, and S. Scopel. Upper bounds on signals due to WIMP self-annihilation: comments on the case of the synchrotron radiation from the galactic center and the WMAP haze. 2008.
- [86] Marco Cirelli, Mario Kadastik, Martti Raidal, and Alessandro Strumia. Model-independent implications of the e+, e-, anti-proton cosmic ray spectra on properties of Dark Matter. 2008.
- [87] T. Delahaye et al. Galactic secondary positron flux at the Earth. *A&A submitted*, 2008.
- [88] T. Delahaye, R. Lineros, F. Donato, N. Fornengo, and P. Salati. Positrons from dark matter annihilation in the galactic halo: Theoretical uncertainties. *Phys. Rev. D*, 77(6):063527–, March 2008.

- [89] T. Delahaye, R. Lineros, F. Donato, N. Fornengo, and P. Salati. Positrons from dark matter annihilation in the galactic halo: theoretical uncertainties. *Phys. Rev.*, D77:063527, 2008.
- [90] F. Donato, N. Fornengo, and D. Maurin. Antideuteron fluxes from dark matter annihilation in diffusion models. *Phys. Rev. D*, 78(4):043506–+, August 2008.
- [91] F. Donato, D. Maurin, P. Brun, T. Delahaye, and P. Salati. Constraints on WIMP Dark Matter from the High Energy PAMELA \bar{p}/p data. 2008.
- [92] Fiorenza Donato, Nicolao Fornengo, and David Maurin. Antideuteron fluxes from dark matter annihilation in diffusion models. *Phys. Rev.*, D78:043506, 2008.
- [93] J. Dunkley et al. Five-Year Wilkinson Microwave Anisotropy Probe (WMAP) Observations: Likelihoods and Parameters from the WMAP data. 2008.
- [94] K. Heitmann, Z. Lukić, P. Fasel, S. Habib, M. S. Warren, M. White, J. Ahrens, L. Ankeny, R. Armstrong, B. O’Shea, P. M. Ricker, V. Springel, J. Stadel, and H. Trac. The cosmic code comparison project. *Computational Science and Discovery*, 1(1):015003–+, October 2008.
- [95] G. Hinshaw et al. Five-Year Wilkinson Microwave Anisotropy Probe (WMAP) Observations: Data Processing, Sky Maps, and Basic Results. 2008.
- [96] J. E. Koglin. Antideuterons as an indirect dark matter signature: design and preparation for a balloon-born GAPS experiment. *JOP:Conference Series, TAUP 2007 Proceedings*, to appear, November 2008.
- [97] E. Komatsu et al. Five-Year Wilkinson Microwave Anisotropy Probe (WMAP) Observations: Cosmological Interpretation. 2008.
- [98] Troy A. Porter, Igor V. Moskalenko, Andrew W. Strong, Elena Orlando, and Laurent Bouchet. Inverse Compton Origin of the Hard X-Ray and Soft Gamma-Ray Emission from the Galactic Ridge. *Astrophys. J.*, 682:400–407, 2008.
- [99] J. Bullock, L. Strigari, and M. Kaplinghat. MW Substructures. *This Volume*, 2009.
- [100] Merritt D. DM at the center of galaxies. *This Volume*, 2009.
- [101] B. Moore and J. Diemand. N-body simulations. *This Volume*, 2009.
- [102] V. S. Berezinskii, S. V. Bulanov, V. A. Dogiel, and V. S. Ptuskin. *Astrophysics of cosmic rays*. Amsterdam: North-Holland, 1990, edited by Ginzburg, V.L., 1990.